Sustainable Carbon Materials

https://doi.org/10.48130/scm-0026-0026

Original Research

Open Access

Sustainable carbon-based composites with integrated toughening and electromagnetic interference shielding performance enabled by Flash-Joule-heating

Jianlong Chen[1], Junchao Ren[1], Mengde Huang[1], Chengyu Yu[1], Shijing Song[1], Yuanyuan Xu[1], Guangbing Zhao[1], Hao Nie[1], Hanwu Lei[2], Deli Zhang[3*] and Qingfa Zhang[1*]

Received: 1 May 2026

Revised: 4 June 2026

Accepted: 26 June 2026

Published online: 28 August 2026

Abstract

Reflection-dominant electromagnetic interference (EMI) shielding materials often suffer from secondary radiation and limited multifunctional integration, highlighting the urgent need for absorption-dominant shielding materials that also possess robust mechanical performance. In this study, a hierarchical layer-by-layer (LBL) PLA/PBAT architecture was developed by integrating Flash-Joule-heated biochar (FJH-BC) with APTES-mediated interfacial regulation to synergistically achieve anisotropic conductive network formation, directional impedance matching, and interfacial toughening. Driven by the synergistic effects of carbon structure optimization and hierarchical assembly, the resulting composite exhibited an outstanding EMI shielding effectiveness of 36.7 dB, featuring an 84% absorption-dominant contribution. Furthermore, the optimized composite achieved a fracture toughness of 2.68 MJ m^{-3} (a 173% increase) and a tensile strength of 25.5 MPa (an 81% increase), together with an electrical conductivity of 12.8 S cm^{-1}. Mechanistic analysis revealed that the LBL architecture facilitated repeated interfacial scattering and prolonged electromagnetic propagation pathways, while the FJH-treated biochar and APTES-mediated interfacial regulation collectively enhanced carrier transport, impedance matching, and stress dissipation. This work establishes a robust structural design strategy for the development of biochar-based sustainable multifunctional composites, achieving the simultaneous optimization of electromagnetic protection and mechanical reinforcement.

Keywords: Layer-by-layer architecture, Flash-Joule heating-treated biochar, Electromagnetic interference shielding, Fracture toughness, Sustainable polymer composites

Highlights

- A layer-by-layer biochar composite architecture was proposed.
- An anisotropic biochar conductive network was constructed.
- Absorption-dominant shielding and fracture toughening were achieved.
- A structural strategy for sustainable composites was established.

* Correspondence: Deli Zhang (zhangdeli@sdut.edu.cn); Qingfa Zhang (zhangqingfa@ahau.edu.cn)

Full list of author information is available at the end of the article.

https://doi.org/10.48130/scm-0026-0026

Graphical abstract

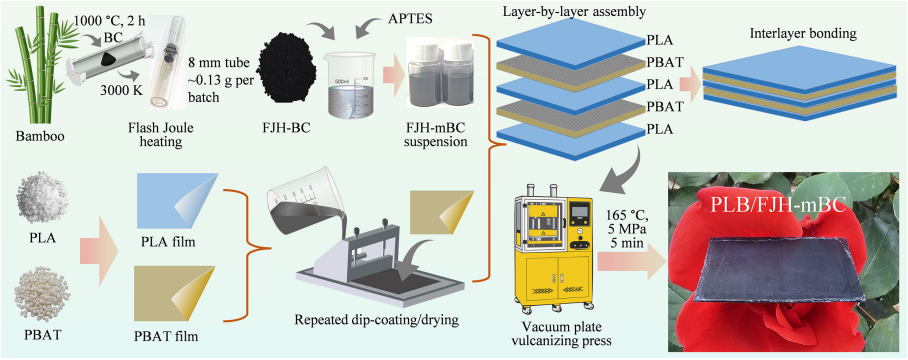

Introduction

With the rapid expansion of wireless communication technologies, portable electronics, and integrated high-frequency systems, electromagnetic interference (EMI) has emerged as a critical issue that threatens device reliability, signal integrity, and information security[1,2]. Conventional EMI shielding materials typically rely on highly conductive networks to attenuate incident electromagnetic waves through reflection[3]. Although such reflection-dominant shielding can provide high shielding effectiveness, excessive reflected waves may generate secondary radiation and compromise electromagnetic stealth, thereby limiting their suitability for advanced electromagnetic protection applications[4–7]. In contrast, absorption-dominant shielding, which promotes electromagnetic wave penetration and internal energy dissipation through conductive loss, dielectric polarization, and multiple scattering, has attracted increasing attention as a promising strategy for mitigating secondary radiation while achieving efficient electromagnetic attenuation[8]. Accordingly, the rational design of materials capable of balancing conductivity, impedance matching, and internal dissipation has become a central focus in the development of next-generation EMI shielding systems[8].

Driven by the increasing demand for lightweight, flexible, and multifunctional electromagnetic protection materials, polymer-based conductive composites have emerged as attractive alternatives to conventional metallic shields owing to their low density, structural versatility, and excellent processability[9]. By incorporating conductive or dielectric fillers into polymer matrices, multiple electromagnetic attenuation mechanisms, including charge transport, interfacial polarization, dipolar relaxation, and multiple scattering, can be effectively activated while preserving the advantages of lightweight structural design[8]. Nevertheless, achieving efficient absorption-dominant EMI shielding in polymer composites remains a significant challenge, as high shielding performance typically relies on the formation of continuous conductive networks through increased filler loading, which often leads to filler aggregation, disrupted phase continuity, weakened interfacial compatibility, and severe impedance mismatch[10]. More importantly, the incorporation of rigid conductive fillers frequently compromises mechanical integrity, resulting in an inherent trade-off between electromagnetic functionality and structural toughness. In this regard, PLA/PBAT blends have attracted considerable attention as sustainable matrices for multifunctional composites because they integrate the high stiffness and renewability of PLA with the excellent ductility and toughness of PBAT, thereby providing a balanced mechanical framework for conductive filler incorporation while maintaining structural stability[11–13]. However, simultaneously realizing efficient absorption-dominant EMI shielding and enhanced fracture toughness in PLA/PBAT composites remains challenging, as conductive network construction, interfacial interaction, and stress-transfer efficiency are often difficult to optimize synergistically[14]. Although recent studies have demonstrated EMI shielding effectiveness values exceeding 20 dB in biochar-based polymer composites, such improvements are frequently accompanied by limited mechanical reinforcement due to filler aggregation and inefficient stress transfer[15–17]. Furthermore, while higher filler loadings can further enhance shielding effectiveness, they often exacerbate the deterioration of mechanical properties, thereby restricting practical applications. Consequently, the development of sustainable composite systems capable of concurrently achieving high-performance EMI shielding and mechanical reinforcement remains highly desirable, highlighting the need for sustainable conductive fillers and interfacial engineering strategies that can simultaneously regulate electromagnetic attenuation pathways, optimize impedance matching, and strengthen mechanical performance.

Biochar-derived conductive fillers have attracted considerable attention for sustainable EMI shielding applications because of their low cost, renewability, and tunable carbon structure[17,18]. Their partially graphitized framework, abundant defects, and porous architecture can facilitate conductive loss, interfacial polarization, and multiple scattering, providing opportunities for electromagnetic attenuation[19]. However, pristine biochar generally exhibits limited graphitization, poor electrical conductivity, and weak filler–matrix interactions, restricting its effectiveness in simultaneously achieving efficient EMI shielding and mechanical reinforcement[20,21]. Flash Joule heating (FJH) has recently emerged as an effective strategy for reconstructing the carbon framework through ultrafast high-temperature treatment, leading to enhanced conductivity and surface activity[22–27]. Nevertheless, the practical utilization of FJH-modified biochar remains constrained by insufficient dispersion and interfacial compatibility in polymer matrices[28]. Surface modification therefore provides a practical approach to improving filler–matrix interactions and structural stability. Among various surface modifiers, APTES is particularly attractive because it can improve filler dispersion and interfacial adhesion through silane-mediated interactions[29].

To address this gap, sophisticated spatial organization of functional fillers has emerged as a powerful design paradigm for simultaneously regulating electromagnetic attenuation pathways and mechanical performance. For instance, multi-layered bi-gradient structures have demonstrated that engineered distribution

gradients can promote electromagnetic wave penetration and internal dissipation, thereby enabling absorption-dominant shielding behavior[30]. Likewise, bio-inspired hierarchical architectures, exemplified by lotus seedpod-inspired core-shell configurations, have revealed the potential of heterogeneous conductive networks to balance shielding effectiveness with structural flexibility[31]. In parallel, conductive interlayers and multi-dimensional hybrid networks have provided additional routes to couple carrier transport with interfacial load transfer, enabling concurrent electromagnetic and mechanical reinforcement[9,32]. Building upon these advances, layer-by-layer (LBL) assembly emerges as a distinctive structural motif for orchestrating programmable filler distribution and anisotropic conductive network formation, while enabling directional impedance regulation, repeated interfacial scattering, and prolonged electromagnetic propagation for enhanced energy dissipation[33,34]. Simultaneously, the layered interfaces can mediate crack deflection, stress redistribution, and interfacial toughening, allowing electromagnetic attenuation and mechanical reinforcement to be coupled through a unified structure-controlled mechanism. Nevertheless, the synergistic integration of FJH-treated biochar, APTES-assisted interfacial regulation, and LBL architecture within sustainable PLA/PBAT composites remains largely unexplored. In the proposed design, FJH-mBC is expected to enhance electrical conductivity and interfacial interactions through carbon framework reconstruction and APTES-assisted surface regulation. The reconstructed carbon framework may facilitate conductive network formation, while the presence of FJH-mBC may also provide potential heterogeneous nucleation sites and promote interfacial stress transfer. Combined with the LBL architecture, these features may provide a promising strategy for simultaneously improving EMI shielding effectiveness and mechanical performance. In this study, a hierarchical LBL polylactide architecture integrating FJH-treated biochar with APTES interfacial regulation is proposed as a coupled structural strategy to establish anisotropic conductive pathways, regulate directional impedance matching, and reinforce interfacial toughening, thereby enabling synergistic absorption-dominant shielding and enhanced fracture toughness in multifunctional sustainable composites.

Materials and methods

Materials

Poly (lactic acid) (PLA, grade 3001D) was supplied by NatureWorks (Minnetonka, MN, USA). Poly (butylene adipate-co-terephthalate) (PBAT) was purchased from BASF (Ludwigshafen, Germany). Bamboo powder was collected from a rural area in Anhui Province, China. 3-aminopropyltriethoxysilane (APTES, purity 99.0%) and acetic acid (AcOH, purity 99.8%) were purchased from Shanghai Aladdin Biochemical Technology Co., Ltd (Shanghai, China). Trichloromethane ($CHCl_3$, purity 99.0%) was supplied by Wuxi Zhanwang Chemical Reagent Co., Ltd. (Wuxi, China). Ethanol was supplied by Tianjin Bohuatong Chemical Products Sales Co., Ltd (Tianjin, China). All chemicals were used as received without further purification.

Preparation of biochar

As shown in Fig. 1a, bamboo powder was first dried at 80 °C for 12 h and then pyrolyzed in a tubular furnace under a nitrogen atmosphere. The temperature was raised to 500 °C at 10 °C min^{-1} and maintained for 30 min, followed by further heating to 1,000 °C and holding for 2 h. After natural cooling to room temperature under nitrogen, the obtained biochar was denoted as BC1000. The BC1000 was then ground and sieved through a 200-mesh sieve. Approximately 0.13 g of the sieved powder was loaded into a quartz reaction tube with graphite electrodes at both ends and subjected to FJH treatment

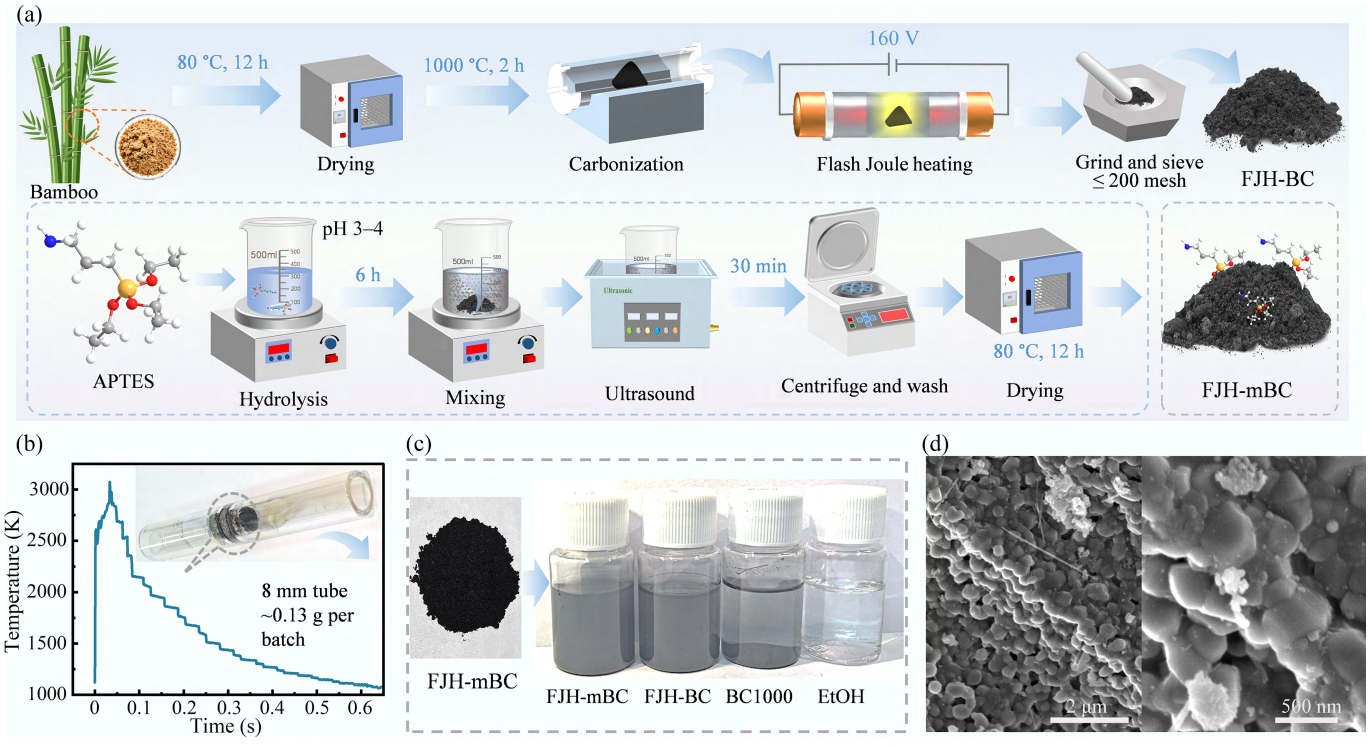

Fig. 1 Fabrication process of FJH-mBC. (**a**) Schematic illustration of the synthesis route; (**b**) Joule heating temperature profile with inset photograph; (**c**) morphology and dispersion comparison; and (**d**) SEM images of FJH-mBC.

https://doi.org/10.48130/scm-0026-0026

(Yidian Technology, China) at 160 V for 0.3 s. This batch size was selected to ensure stable electrical discharge and reproducible processing under laboratory-scale conditions. The transient temperature during the FJH process was approximately 3,000 K (Fig. 1b). After natural cooling to room temperature, the product was ground, sieved, and designated as FJH-BC. For surface modification, 2 wt.% APTES was added to an ethanol/water mixture (95:5, v/v), and the pH was adjusted to 3–4 using acetic acid. FJH-BC was introduced into the solution, followed by magnetic stirring at room temperature for 6 h and ultrasonication for 30 min (Fig. 1a). The product was then collected by centrifugation (10,000 rpm, 5 min), washed twice with ethanol, and dried at 80 °C for 12 h to obtain the modified FJH-BC, denoted as FJH-mBC.

Preparation of PLB/FJH-mBC composites

PLA and PBAT pellets were dried at 50 °C for 12 h prior to processing. PLA films were prepared by hot pressing PLA pellets using a vacuum hot press (SY-6210-BZ-30T, Shiyan Precision Instruments Co., Ltd., China) at 185 °C under 1.5 MPa for 2 min, followed by pressing at 5 MPa for 3 min. PBAT films were prepared by hot pressing PBAT pellets at 145 °C under 1.5 MPa for 3 min, followed by pressing at 5 MPa for 5 min. A layered PLA/PBAT matrix (PLB) was constructed via stepwise LBL assembly. The PLA/PBAT mass ratio was fixed at 6:4, and the overall composition of the PLB matrix was maintained by controlling the mass of each individual film layer. PLA and PBAT films were alternately stacked in a PLA/PBAT/PLA/PBAT/PLA sequence to form a five-layer structure, which was preheated at 165 °C under 1.5 MPa for 3 min, hot-pressed at 5 MPa for 5 min, and cold-pressed for 30 min to obtain the PLB matrix. As a control, PLA and PBAT at the same mass ratio were dissolved in chloroform and subjected to slow solvent evaporation and vacuum drying; the resulting non-layered PLB sample was denoted as PLA/PBAT. For composite fabrication, BC1000, FJH-BC, or FJH-mBC was dispersed in ethanol to form a suspension at 5 mg mL^{-1}. The suspension was uniformly coated onto PBAT film surfaces, and a uniform PBAT-BC layer with a filler content of 10 wt.% was obtained through multiple coating-drying cycles by controlling the coating amount. The coated films were then assembled following the same PLA/PBAT alternating sequence to construct a symmetric layered structure in which biochar was distributed at the interfacial regions between PLA and PBAT layers. The assembled structure was subjected to vacuum hot pressing at 165 °C under 1.5 MPa for 3 min, followed by pressing at 5 MPa for 5 min and cold pressing for 30 min, yielding PLB/BC, PLB/FJH-BC, and PLB/FJH-mBC composites.

Characterization and property evaluation

FTIR was employed to analyze the surface functional groups of biochar and the chemical structures of composite samples. For biochar characterization, spectra were recorded on a Nicolet 6700 spectrometer (Thermo Nicolet, USA) using the KBr pellet method over the wavenumber range of 4,000–400 cm^{-1}, with a resolution of 4 cm^{-1} and 64 scans per sample. For composite characterization, spectra were collected on the same instrument equipped with an ATR accessory in the range of 4,000–500 cm^{-1} at a resolution of 4 cm^{-1} with 32 scans per measurement, and were used to evaluate chemical structure and interfacial interactions. XRD was used to analyze the crystalline structures of biochar and composite samples using a SmartLab SE diffractometer (Rigaku, Japan) equipped with Cu Kα radiation (λ = 0.154 nm) at a scanning rate of 5° min^{-1}. Diffraction patterns were recorded over a 2θ range of 5°–80° for biochar and 5°–50° for composite samples to evaluate crystalline structure and phase composition. Raman spectroscopy was employed to analyze the graphitic structure and defect characteristics of biochar using a Raman spectrometer (LabRAM HR Evolution, Horiba-Jobin Yvon, France) with a 532 nm excitation laser. Raman spectra were collected over a Raman shift range of 800–3,000 cm^{-1}. X-ray photoelectron spectroscopy (XPS) was used to analyze the surface elemental composition and chemical states of the biochar using a K-Alpha spectrometer (Thermo Scientific, USA) equipped with a monochromatic Al Kα X-ray source (hν = 1,486.6 eV). Survey spectra were recorded over a binding energy range of 0–1,350 eV with a pass energy of 100 eV, while high-resolution spectra were acquired at a pass energy of 50 eV. Charge neutralization was applied, and all binding energies were calibrated using the C1s peak at 284.8 eV. Scanning electron microscopy (SEM) was used to examine the morphology of biochar and the fractured surfaces of composites using a scanning electron microscope (Quanta 250, USA). Observations were conducted at an accelerating voltage of 10 kV after gold sputter coating. TGA was conducted to evaluate the thermal stability and decomposition behavior of composite samples using a TG 209 F1 instrument (NETZSCH-Gerätebau GmbH, Germany). Measurements were conducted from room temperature to 800 °C at a heating rate of 10 °C min^{-1} under a nitrogen atmosphere. Derivative thermogravimetric (DTG) curves were obtained from the first derivative of weight loss with respect to temperature. DSC was employed to analyze the thermal transition behavior of composite samples using a DSC 214 Polyma instrument (Netzsch Group, Germany) under a nitrogen flow of 50 mL min^{-1}. Measurements were conducted at a heating/cooling rate of 10 °C min^{-1} using a heat-cool-heat program. Samples were first heated from room temperature to 180 °C and held for 3 min to eliminate thermal history, then cooled to −50 °C to record the crystallization temperature (Tc), followed by a second heating scan from −50 to 200 °C to determine the glass transition temperature (Tg) and melting temperature (Tm). Electrical conductivity was measured using a four-point probe instrument (RTS-8, China). Infrared thermal imaging was used to record the surface temperature distribution of the composite samples under applied voltage using an infrared thermal imaging camera (E4, FLIR Systems, USA). The EMI shielding performance of the composite samples was measured using a vector network analyzer (Agilent N5232A, USA) in the X-band (8.2–12.4 GHz). Composite specimens were machined to the required waveguide dimensions and inserted into the test fixture for measurement. The total shielding effectiveness (SE_T), reflection loss (SE_R), and absorption loss (SE_A) were determined according to the following Eqs (1)–(6):

$$R = |S_{11}|^2 \tag{1}$$

$$T = |S_{21}|^2 \tag{2}$$

$$\mathrm{A} = 1 - \mathrm{R} - \mathrm{T} \tag{3}$$

$$SE_T = 10\lg\left(\frac{1}{T}\right) \tag{4}$$

$$SE_R = 10\lg\left(\frac{1}{1-R}\right) \tag{5}$$

$$SE_A = 10\lg\left(\frac{1-R}{T}\right) \tag{6}$$

where, R, T, and A represent the reflection, transmission, and absorption coefficients, respectively, and the multiple reflection term (SE_M) was neglected when SE_T > 15 dB. The mechanical properties of the composite samples were measured using a universal testing machine (UTM4104X, Sunstest Co., Ltd, China) equipped with a 500 N load cell. Tensile tests were conducted at a crosshead speed of 20 mm min^{-1} using specimens with a gauge length of 30 mm. Five specimens were tested for each sample, and the tensile strength, elongation at break,

Young's modulus, and fracture toughness were obtained from the stress–strain curves.

Results and discussion

Structural characterization of FJH-mBC

The structural evolution of FJH-mBC was first investigated based on the FJH process and the resulting morphological characteristics, as shown in Fig. 1b–d. A rapid temperature rise to ~3,000 K within a short duration is observed in Fig. 1b under the applied voltage, reflecting an ultrafast heating process that drives carbon reconstruction and conductive network formation. The dispersion behavior of the samples in ethanol is presented in Fig. 1c. BC1000 shows pronounced sedimentation, indicating poor dispersion stability. In contrast, FJH-BC exhibits improved dispersion, while FJH-mBC forms a uniform and stable suspension without noticeable aggregation. This behavior indicates enhanced interfacial affinity between the modified carbon surface and ethanol, which is favorable for subsequent processing. The SEM image (Fig. 1d) shows a rough and interconnected morphology with irregular surface features, indicating a high surface complexity that is favorable for interfacial contact. To further elucidate the evolution of surface functionalities, FTIR spectra were analyzed (Fig. 2a). All samples share similar spectral features, including a broad band at ~3,429 cm^{-1} attributed to O–H stretching vibrations, peaks at 2,926 and 2,853 cm^{-1} corresponding to aliphatic C–H stretching, and bands at 1,633, 1,461, and 1,383 cm^{-1} associated with carbon framework vibrations. After FJH treatment, the intensity of the O–H band decreases, suggesting partial removal of oxygen-containing functionalities under ultrafast high-temperature conditions. Compared with FJH-BC, FJH-mBC shows a slight enhancement in the 1,000–1,200 cm^{-1} region, which is attributed to the introduction of Si–O-related structures after APTES modification. Meanwhile, the overall spectral features exhibit minimal variation, indicating that the modification predominantly alters surface chemistry while preserving the carbon framework. The XRD patterns (Fig. 2b) show that all samples exhibit a broad peak at $2\theta \approx 26.7°$, corresponding to the (002) plane of partially ordered carbon, indicating a predominantly disordered carbon structure. After FJH treatment, this peak becomes slightly sharper, suggesting a modest increase in structural ordering. In addition, several sharp diffraction peaks appear at approximately 35.7°, 41.5°, 60.0°, 71.8°, and 75.6°, which can be tentatively indexed to the (111), (200), (220), (311), and (222) planes of cubic Si-containing phases (e.g., β-SiC, PDF No. 29-1129)[35], primarily originating from the intrinsic silicon species in bamboo. After APTES modification, no new diffraction peaks are observed, indicating that the surface functionalization does not alter the bulk crystalline structure of FJH-BC. The Raman spectra of the samples are shown in Fig. 2c. All samples exhibit two characteristic bands at around 1,340 cm^{-1} (D band) and 1,580 cm^{-1} (G band), which are associated with disordered carbon structures and graphitic domains, respectively. Compared with BC, the D and G bands of FJH-BC become more distinct, with increased intensity and reduced peak broadening. A similar feature is observed for FJH-mBC, where the two bands are more clearly resolved. The calculated ID/IG values were 0.94, 1.03, and 1.44 for BC, FJH-BC, and FJH-mBC, respectively, indicating carbon framework reconstruction during FJH treatment, while the enhanced conductivity was likely related to conductive domain reconstruction and the removal of insulating species. The surface chemical composition was further analyzed by XPS (Fig. 2d–g). The survey spectra (Fig. 2d) show that BC mainly contains C, O, and Si elements, while an additional N signal appears in FJH-mBC, indicating the introduction of nitrogen-containing functional groups. The high-resolution C1s spectra (Fig. 2e) can be deconvoluted into components corresponding to C–C/C=C and C–O bonds. Compared with BC, FJH-BC shows a reduced contribution of oxygen-containing groups, suggesting partial removal of surface functionalities. FJH-mBC exhibits an additional C–N component, which is attributed to APTES-derived species. The O1s spectra (Fig. 2f) exhibit contributions from C–O, C=O, and –OH groups. Compared with BC, FJH-BC shows a reduced contribution of the –OH component, suggesting partial removal of hydroxyl groups. In contrast, FJH-mBC exhibits an increased relative intensity of the –OH-related component, which is attributed to the introduction of surface functional groups during APTES modification. The N1s signal (Fig. 2g) is negligible for BC and FJH-BC but becomes evident in FJH-mBC, further supporting the successful introduction of nitrogen-containing functional groups. The high-resolution Si2p spectra (Supplementary Fig. S1) reveal the coexistence of Si–O–Si, Si–O–C, and Si–C species. The increased Si–O–Si and Si–O–C contributions after APTES modification confirm successful silane grafting, which is expected to improve interfacial compatibility between FJH-mBC and the PLA/PBAT matrix. Based on the above structural and chemical analyses, a schematic illustration of the proposed interfacial interactions between silane-derived species and the carbon surface is presented in Fig. 2h. Upon hydrolysis, APTES was converted into silanol species, which could interact with the carbon surface through multiple pathways. Si–O–C bonding was considered to anchor silane molecules onto the carbon surface, while hydrogen bonding between surface hydroxyl groups and silanol species may further contribute to interfacial affinity[36]. In addition, electrostatic interactions between polar groups and the carbon surface were also involved. Meanwhile, π–π stacking interactions between the carbon framework and organic moieties may have occurred[20]. These interactions collectively enhanced interfacial compatibility and facilitated a uniform dispersion of the modified biochar.

Structural characterization of PLB composites

As illustrated in Fig. 3a, a layer-by-layer (LBL) assembly strategy was employed to construct PLA/PBAT composites with a controlled interfacial architecture. In this design, FJH-mBC was selectively introduced as an interfacial functional layer between PLA and PBAT films, forming a sandwich-like multilayer structure. Such a design enables regulated interfacial interactions and improved interlayer connectivity. The FTIR spectra (Fig. 3b) exhibit similar characteristic absorption bands for all samples. The peak at 1,748 cm^{-1} is assigned to C=O stretching of ester groups, originating from both PLA and PBAT. Bands in the 1,000–1,200 cm^{-1} region are attributed to C–O–C vibrations, primarily associated with PLA, whereas the bands at 1,456 and 1,383 cm^{-1} correspond to CH_2 bending vibrations, mainly arising from PBAT segments. Overall, the spectral features remain largely unchanged, indicating that the polymer structure is preserved. The slight variations in band intensity are nevertheless observed, with more pronounced changes in PLB/FJH-mBC, particularly around 1,000–1,200 and 1,400 cm^{-1}, whereas PLB/FJH-BC shows weaker variations. This difference suggests relatively stronger interfacial interactions in PLB/FJH-mBC. The XRD patterns of the PLB composites are shown in Fig. 3c. The diffraction peaks at 14.8°, 16.7°, 19.0°, and 22.4° are assigned to the (110), (110)/(200), (203), and (210) planes of PLA[37], while those at 23.1° and 24.9° correspond to the (110) and (020) planes of PBAT[38]. Upon the incorporation of biochar, the characteristic diffraction peaks exhibit a marked increase in intensity. Additional peaks at 12.4°, 29.1°, 31.2°, and 35.6° are observed and are tentatively attributed to crystalline inorganic phases derived from the biochar. The feature at 35.6° may be associated with a (111) reflection of Si-containing or mineral-derived

https://doi.org/10.48130/scm-0026-0026

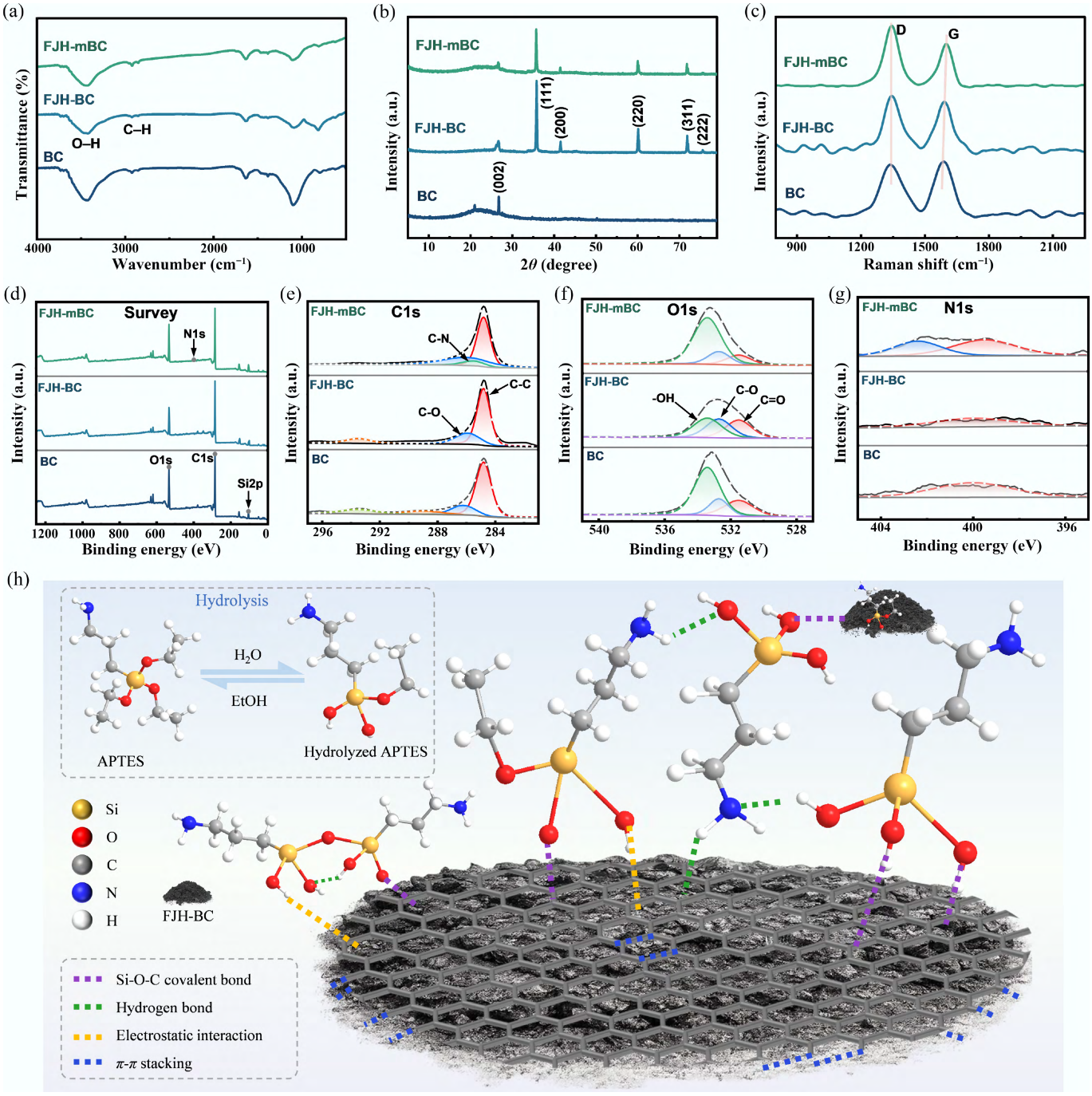

Fig. 2 Structural characterization and interaction mechanism of FJH-mBC. (**a**) FTIR spectra; (**b**) XRD patterns; (**c**) Raman spectra; (**d**) XPS survey spectra and corresponding high-resolution spectra of (**e**) C1s, (**f**) O1s, and (**g**) N1s; and (**h**) schematic illustration of interfacial interactions.

phases. These results indicate that the polymer crystalline framework is preserved while additional crystalline features are introduced. Based on the above structural analyses, a schematic illustration of the interfacial interactions within the PLB composites is presented in Fig. 3d. In the LBL architecture, FJH-mBC was located at the interface between PLA and PBAT layers, forming a continuous interfacial region. As illustrated, Si–O–C linkages were considered to anchor the modified biochar onto the polymer interface, while hydrogen bonding interactions occurred between surface functional groups and the polar segments of PLA and PBAT chains[36]. The presence of these interactions enhanced interfacial adhesion, and the layered configuration further improved interfacial contact, thereby facilitating stress transfer across adjacent layers[33]. These combined effects contributed to improved interfacial compatibility within the composite system.

Mechanical properties

The mechanical properties of the PLB composites were evaluated to further assess the effectiveness of the interfacial design, as shown in Fig. 4. The stress–strain curves are presented in Fig. 4a, where PLA/PBAT exhibits relatively low strength and limited elongation at

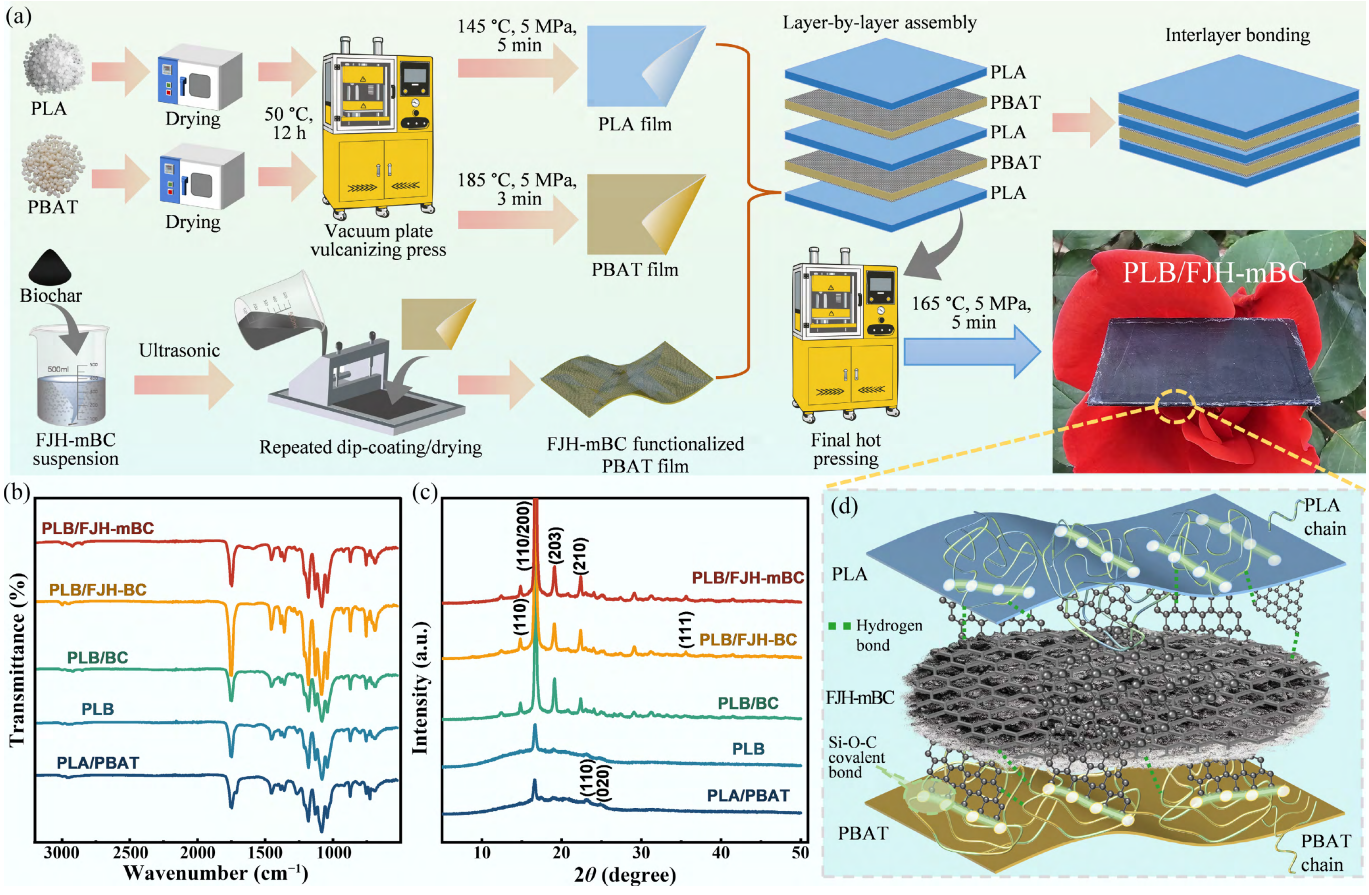

Fig. 3 Fabrication, structural characterization, and interfacial interactions of PLB composites. (**a**) Schematic illustration of the preparation process; (**b**) FTIR spectra; (**c**) XRD patterns; and (**d**) schematic illustration of interfacial interactions.

break. With the incorporation of biochar, both tensile strength and elongation are improved to varying extents. Among all samples, PLB/FJH-mBC achieves the highest elongation at break while maintaining a high tensile strength, reflecting a simultaneous enhancement in strength and ductility. In contrast, PLB/BC undergoes earlier fracture with lower elongation, whereas PLB/FJH-BC exhibits an intermediate improvement. For comparison, a conventionally solution-cast PLA/PBAT/FJH-mBC blend exhibits lower tensile strength and elongation than PLB/FJH-mBC, indicating that the superior mechanical performance cannot be achieved by filler incorporation alone. According to Fig. 4b, the tensile strength increases progressively with the incorporation and modification of biochar, and PLB/FJH-mBC exhibits the best performance among all samples. Specifically, the tensile strength of PLA/PBAT, PLB/BC, PLB/FJH-BC, and PLB/FJH-mBC is 14.1, 18.4, 20.8, and 25.5 MPa, respectively. Compared with PLA/PBAT, the tensile strength of PLB/FJH-mBC is increased by approximately 81%. The improvement in tensile strength can be associated with enhanced interfacial interactions and improved dispersion of the modified biochar within the polymer matrix. In contrast, the relatively lower strength of PLB/BC suggests less effective interfacial interaction, while PLB/FJH-BC shows an intermediate improvement. The tensile modulus (Fig. 4c) also exhibits a gradual increasing trend with the incorporation of biochar, and PLB/FJH-mBC shows the highest stiffness among all samples. Specifically, the tensile modulus of PLA/PBAT, PLB/BC, PLB/FJH-BC, and PLB/FJH-mBC is 195.4, 218.4, 242.6, and 285.2 MPa, respectively. Compared with PLA/PBAT, the modulus of PLB/FJH-mBC is increased by approximately 46%. This result suggests that the introduction of biochar, particularly FJH-mBC, enhances the rigidity of the composite. The elongation at break (Fig. 4d) shows a significant improvement after the incorporation of biochar. PLA/PBAT exhibits a relatively low elongation of 11.5%, whereas PLB/FJH-mBC reaches 24.7%, corresponding to an increase of approximately 115%. PLB/BC and PLB/FJH-BC exhibit intermediate values of 14.5% and 17.4%, respectively. This behavior indicates that the modified biochar not only reinforces the matrix but also improves ductility, suggesting a more effective stress distribution within the composite system. As summarized in Fig. 4e, the toughness follows a similar trend to the elongation at break. The toughness increases from 0.98 MJ m^{-3} for PLA/PBAT to 1.43 MJ m^{-3} and 2.07 MJ m^{-3} for PLB/BC and PLB/FJH-BC, respectively, and further reaches 2.68 MJ m^{-3} for PLB/FJH-mBC. This corresponds to an increase of approximately 173% compared with PLA/PBAT. The substantial enhancement in toughness reflects the synergistic improvement in both strength and ductility, which is more pronounced in PLB/FJH-mBC. Overall, PLB/FJH-mBC achieves the most balanced enhancement in strength, stiffness, and ductility among all samples. As shown in Fig. 4f, compared with previously reported PLA/PBAT-based composites, PLB/FJH-mBC exhibits higher improvement ratios in both tensile strength and elongation at break[11,39–44]. This result indicates that the incorporation of FJH-mBC, together with the LBL interfacial design, enables a more efficient synergy between strength and ductility, which is rarely achieved in conventional PLA/PBAT-based systems. The fracture morphologies (Fig. 4g) show a transition from a smooth, brittle surface in PLA/PBAT to increasingly rough and tortuous surfaces with biochar incorporation. PLB/FJH-mBC

https://doi.org/10.48130/scm-0026-0026

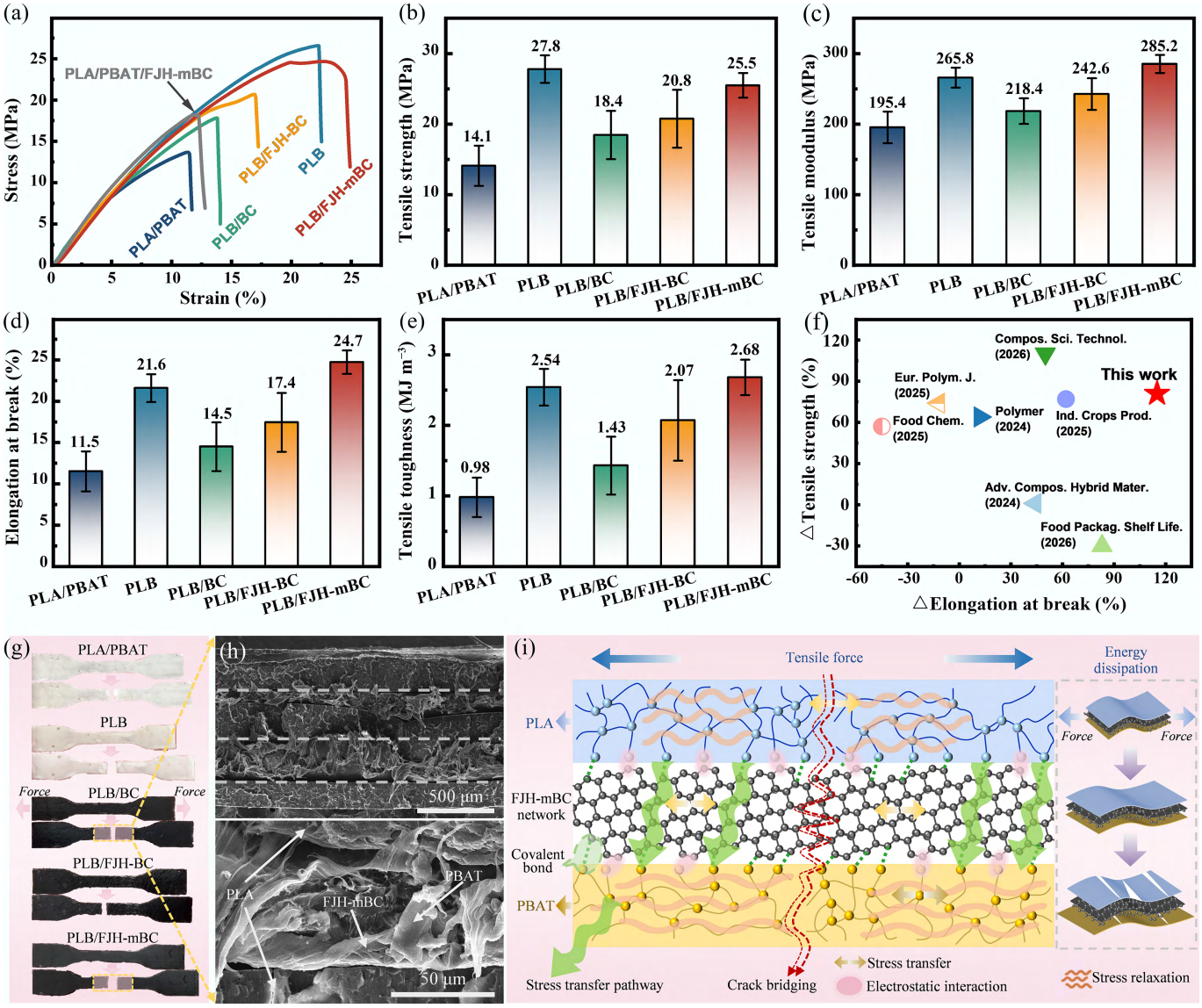

Fig. 4 Mechanical performance and toughening mechanism of PLB composites. (**a**) Stress–strain curves; (**b**) tensile strength; (**c**) tensile modulus; (**d**) elongation at break; (**e**) toughness; (**f**) comparison with reported materials; (**g**) fracture photographs; (**h**) SEM images; and (**i**) schematic illustration of the toughening mechanism.

exhibits the most pronounced roughness and plastic deformation features, indicating enhanced energy dissipation during fracture. To further examine the fracture features, SEM images of PLB/FJH-mBC are presented in Fig. 4h. The cross-sectional morphology reveals a well-defined layered structure, as highlighted by the dashed lines, indicating the successful construction of the LBL architecture. At higher magnification, FJH-mBC is clearly located at the interface between PLA and PBAT phases, forming a continuous interfacial region without evident agglomeration. Notably, interconnected and bridging-like features are observed across adjacent layers, together with pronounced plastic deformation and fibrillar structures. These characteristics suggest that crack propagation is effectively deflected and constrained along a tortuous path, which is favorable for energy dissipation during fracture. Based on the above mechanical and morphological analyses, a schematic illustration of the strengthening and toughening mechanism is presented in Fig. 4i. This interfacial architecture positioned FJH-mBC between PLA and PBAT layers, forming a continuous interfacial region. The interfacial design enabled efficient stress redistribution across adjacent layers and enhanced interlayer connectivity[33]. Under tensile loading, the applied stress was redistributed through the interfacial region, which delayed crack initiation. As deformation proceeded, the layered structure promoted crack deflection and bridging along a tortuous propagation path[45]. Meanwhile, localized deformation and interfacial interactions contributed to stress relaxation and energy dissipation[45]. These combined effects resulted in the simultaneous enhancement of strength, stiffness, and ductility observed in PLB/FJH-mBC.

Thermal and energy conversion properties

Thermal stability is a critical prerequisite for the reliable electro-thermal operation and practical application of functional composites. The thermal degradation behaviors and energy conversion properties of

the composites are presented in Fig. 5. The thermogravimetric (TG) curves (Fig. 5a) reveal a primary continuous weight loss stage between approximately 260 and 440 °C, corresponding to the thermal decomposition of the PLA/PBAT matrix. A slight mass loss below 200 °C is attributed to the evaporation of absorbed moisture and residual volatile species. Correspondingly, the DTG curves (Fig. 5b) exhibit two characteristic degradation peaks associated with the decomposition of the PLA-rich and PBAT-rich phases. Compared with PLB, the first degradation peak shifts from approximately 297 to 343 °C after the incorporation of FJH-mBC, indicating a delayed thermal degradation process and enhanced thermal stability of the composite. To further elucidate the influence of the hierarchical carbon network on the phase transition behaviors, differential scanning calorimetry (DSC) was conducted. The cooling curves (Fig. 5c) reveal that the incorporation of biochar significantly alters the crystallization process of the polymer matrix. For pure PLB, only a single crystallization peak is observed, which can be attributed to the overlapping crystallization processes of the PLA and PBAT phases. With the incorporation of biochar, the crystallization behavior becomes more distinguishable. For PLB/FJH-mBC, two distinct crystallization peaks (Tc_1 and Tc_2) are observed, indicating that FJH-mBC acts as an efficient heterogeneous nucleating agent and promotes crystallization by providing abundant nucleation sites, resulting in a more differentiated crystallization behavior of the polymer phases[46]. Correspondingly, the heating curves (Fig. 5d) demonstrate a high degree of consistency across all samples. The glass transition temperature (Tg, ~60 °C), melting temperature (Tm, ~167 °C), and the overall endothermic peak profiles remain largely invariant regardless of the biochar incorporation. This uniform thermal behavior indicates that the introduction of the hierarchical carbon network does not disrupt the inherent crystalline domains or severely restrict the segmental mobility of the PLA/PBAT matrix. Consequently, the incorporation of FJH-mBC and the LBL architecture does not significantly alter the intrinsic thermal transition behavior of the PLA/PBAT matrix while enabling the formation of an electrically conductive network. To evaluate the electrothermal performance of the composites, the Joule heating behavior of PLB/FJH-mBC was further investigated. As shown in Fig. 5e, the surface temperature increased rapidly with increasing applied voltage and gradually reached a stable equilibrium state, demonstrating a voltage-dependent electrothermal response. The equilibrium temperature increased from approximately 25 to 58 °C as the applied voltage increased from 3 to 9 V. Furthermore, the equilibrium surface temperature exhibited an approximately linear

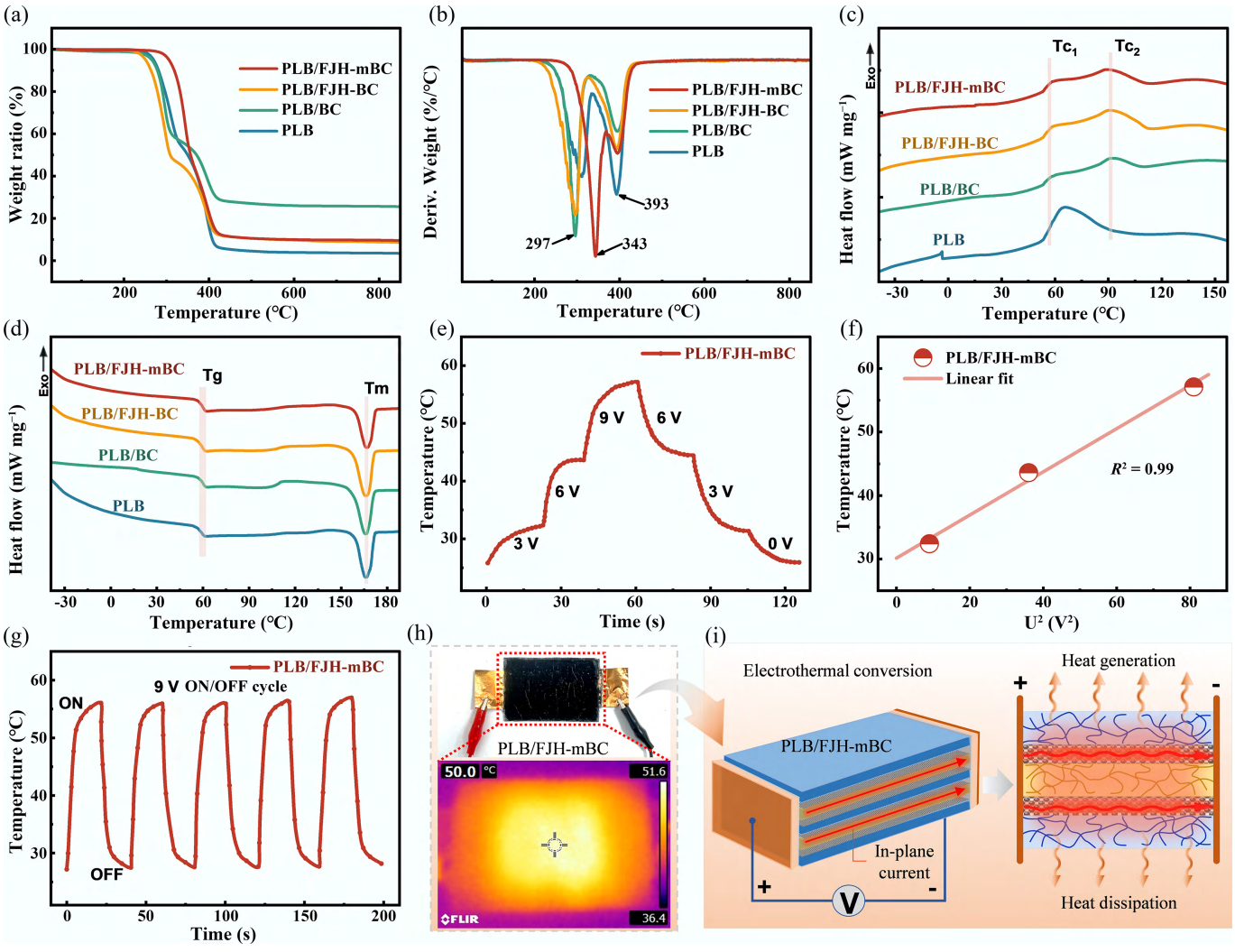

Fig. 5 Thermal and electrothermal properties of PLB composites. (**a**) TG curves; (**b**) DTG curves; (**c**) DSC cooling curves; (**d**) DSC heating curves; (**e**) temperature evolution curves under different applied voltages; (**f**) linear fitting of surface temperature vs U^2; (**g**) electrothermal cycling stability; (**h**) IR image; and (**i**) schematic illustration of the Joule heating mechanism.

https://doi.org/10.48130/scm-0026-0026

relationship with U^2 (Fig. 5f), which is consistent with the Joule heating mechanism and indicates efficient electrothermal energy conversion within the conductive network. To evaluate the stability of the electrothermal performance, cyclic ON/OFF measurements were conducted under an applied voltage of 9 V. As shown in Fig. 5g, the maximum temperature remained nearly unchanged during five consecutive heating–cooling cycles, indicating excellent electrothermal cycling stability and robust conductive network integrity. The infrared (IR) thermal image shown in Fig. 5h further demonstrates a highly uniform temperature distribution across the entire sample surface without obvious local hot spots. This thermal uniformity can be attributed to the homogeneous distribution of FJH-mBC and the formation of a continuous conductive pathway within the LBL architecture. The corresponding electrothermal conversion mechanism is schematically illustrated in Fig. 5i. Upon application of an external electric field, electrons are transported through the interconnected conductive pathways constructed by FJH-mBC within the layered structure. Electrical energy is subsequently converted into thermal energy through the Joule effect, while the generated heat is uniformly dissipated throughout the adjacent PLA/PBAT matrix. The synergistic combination of the conductive network and layered architecture therefore enables efficient electrothermal conversion and stable thermal output.

EMI shielding performance

As shown in Fig. 6a, the insulating nature of PLA/PBAT and PLB was effectively overcome upon biochar incorporation, leading to a pronounced increase in conductivity due to the formation of percolated conductive pathways. Specifically, the electrical conductivity values for PLB/BC, PLB/FJH-BC, and PLB/FJH-mBC were 1.7, 8.5, and 12.8 S cm^{-1}, respectively. This enhancement was ascribed to the high graphitization degree of FJH-mBC and the well-defined, continuous 3D conductive network enabled by the LBL architecture, which underpinned the improved EMI shielding performance. As shown in Fig. 6b, the EMI shielding performance was evaluated in the X-band (8.2–12.4 GHz). The SE_T scales positively with conductivity, consistent with the enhanced charge transport. The average SE_T increases from 19.28 dB (PLB/BC) to 31.48 dB (PLB/FJH-BC) and 36.7 dB (PLB/FJH-mBC), with the latter significantly exceeding the 20 dB threshold for commercial

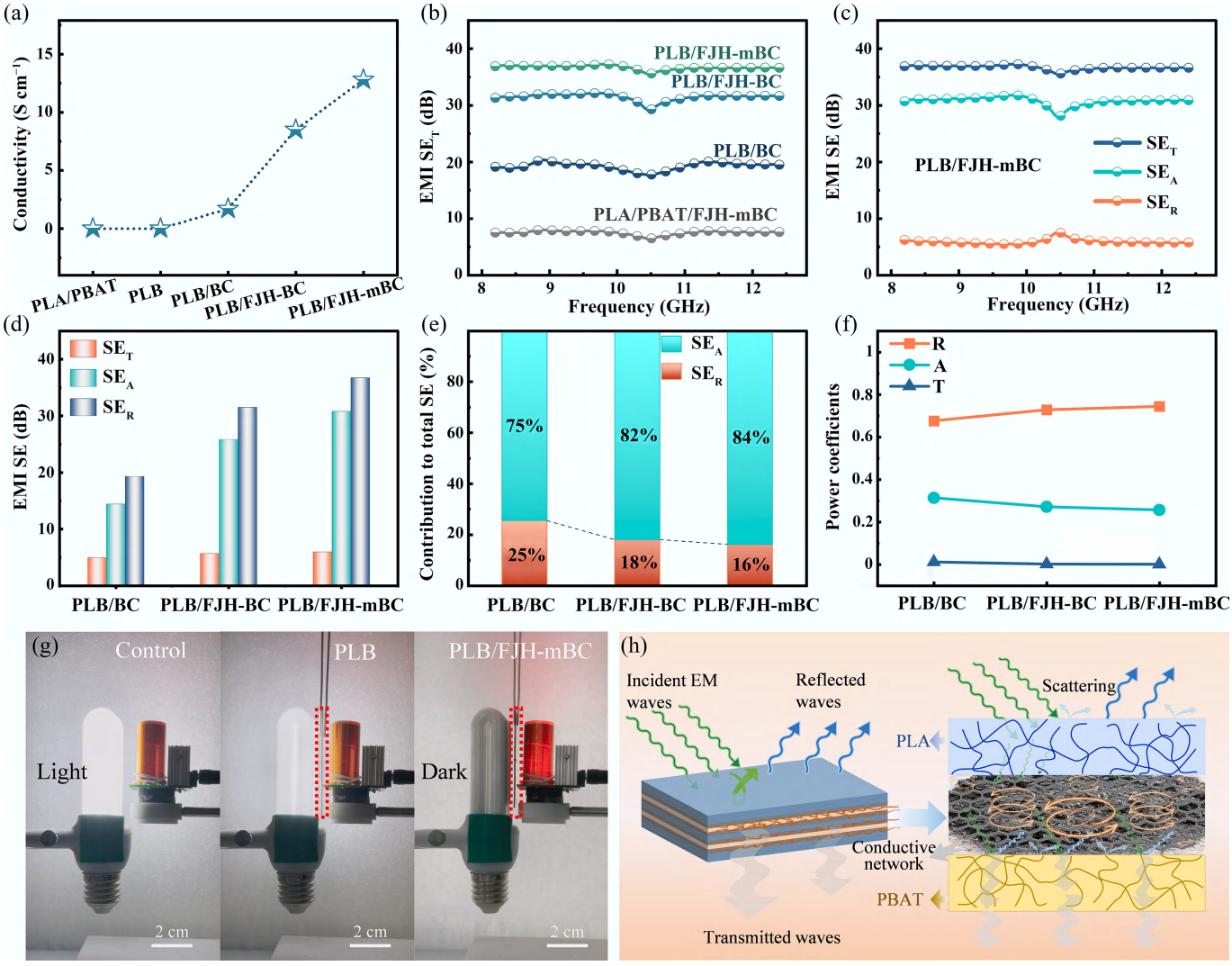

Fig. 6 Electrical conductivity, EMI shielding performance, and mechanism of PLB composites. (**a**) Conductivity; (**b**) EMI SE of different samples; (**c**) SE components of the optimal sample; (**d**) SE decomposition; (**e**) contribution to total SE; (**f**) power coefficients; (**g**) EMI shielding demonstration; and (**h**) shielding mechanism illustration.

applications[47]. For comparison, a conventionally solution-cast PLA/PBAT/FJH-mBC blend containing the same filler loading (10 wt.%) exhibited an average SE_T of only 7.5 dB, highlighting the critical role of the LBL architecture in constructing efficient conductive pathways for electromagnetic attenuation. In addition, the SE_T remains nearly frequency-independent across the X-band, indicating stable and reliable shielding enabled by the LBL architecture. To elucidate the attenuation mechanism, the SE_T was decomposed into SE_R and SE_A. As shown in Fig. 6c, for PLB/FJH-mBC, SE_A (30.8 dB) markedly exceeds SE_R (5.9 dB), indicating absorption-dominated shielding. This behavior is consistent across all samples (Fig. 6d), where SE_A increases from 14.4 dB (PLB/BC) to 30.8 dB (PLB/FJH-mBC), while SE_R remains low and nearly invariant (4.9–5.9 dB). These results confirm that the enhanced shielding performance primarily arises from improved energy dissipation within the optimized hierarchical carbon network. Although partial surface reflection still exists, absorption remains the dominant contribution to the overall shielding effectiveness. The quantitative contribution of each shielding component was further elucidated in Fig. 6e. The contribution of SE_A increases from 75% (PLB/BC) to 84% (PLB/FJH-mBC), while SE_R decreases from 25% to 16%, confirming the evolution toward absorption-dominated shielding with hierarchical network optimization. This behavior is corroborated by the power coefficients (Fig. 6f). For PLB/FJH-mBC, the transmission coefficient (T) is suppressed to 2.1×10^{-4}, indicating near-complete attenuation of incident waves. Despite a relatively high reflection coefficient ($R \approx 0.74$), the negligible T confirms that the electromagnetic waves entering the composite are effectively confined and dissipated within the internal structure via the synergistic effects of the LBL architecture and FJH-mBC. This is consistent with the absorption-dominated shielding behavior indicated by the SE_A and SE_R analysis. A macroscopic circuit test was performed to demonstrate practical shielding capability (Fig. 6g). While the indicator bulb remained brightly illuminated when a pure PLB film was employed, it was immediately extinguished upon the insertion of the PLB/FJH-mBC composite, confirming the exceptional reliability of the material in blocking electromagnetic radiation. The underlying electromagnetic attenuation mechanism was schematically illustrated in Fig. 6h. Upon reaching the air-composite interface, a fraction of the incident electromagnetic waves was reflected due to the impedance mismatch. The remaining waves penetrated into the labyrinth-like LBL architecture, where an interconnected conductive network formed by the highly graphitized FJH-mBC enabled the efficient conversion of electromagnetic energy into thermal energy via intense conduction loss. Simultaneously, the alternating layered configuration and abundant heterogeneous interfaces facilitated multiple internal reflections and interfacial polarization. Consequently, the incident energy was synergistically dissipated through conduction loss, polarization relaxation, and multiple scattering, endowing the PLB/FJH-mBC composite with superior EMI shielding performance.

Conclusions

In this study, FJH-mBC was synthesized from bamboo biochar via FJH and APTES modification, and subsequently incorporated into a PLA/PBAT matrix through LBL assembly to construct hierarchical PLB/FJH-mBC composites. The anisotropic conductive network formation and interfacial regulation mechanisms were elucidated, revealing that the well-defined LBL architecture and highly graphitized biochar jointly facilitated carrier transport, enhanced interfacial stress transfer, and optimized impedance matching. As a result, the optimized composite achieved a remarkable fracture toughness of 2.68 MJ m^{-3} and a tensile strength of 25.5 MPa, corresponding to increases of 173% and 81% relative to the pure PLA/PBAT matrix. In addition, the composite delivered an electrical conductivity of 12.8 S cm^{-1} and an EMI shielding effectiveness of 36.7 dB (84% absorption), confirming its absorption-dominant attenuation behavior. These combined enhancements effectively address key challenges in sustainable shielding materials, including the stiffness–toughness trade-off and excessive secondary electromagnetic radiation, positioning biochar-based LBL architectures as efficient and sustainable platforms for multifunctional composites. The PLB/FJH-mBC composites, featuring excellent mechanical, EMI shielding, and Joule-heating performance, hold strong potential for advanced functional-material technologies and sustainable structural applications.

Supplementary information

It accompanies this paper at: https://doi.org/10.48130/scm-0026-0026.

Ethical statements

Not applicable.

Author contributions

The authors confirm their contributions to the paper as follows: Jianlong Chen: conceptualization, methodology, investigation, data curation, formal analysis, writing—original draft; Junchao Ren: investigation, data curation, formal analysis; Mengde Huang: investigation, data curation; Chengyu Yu: investigation; Shijing Song: investigation; Yuanyuan Xu: investigation; Guangbing Zhao: resources; Hao Nie: resources; Hanwu Lei: supervision, visualization; Deli Zhang: supervision, funding acquisition, writing—review and editing; Qingfa Zhang: supervision, funding acquisition, project administration, writing—review and editing. All authors reviewed the results and approved the final version of the manuscript.

Data availability

All data generated or analyzed during this study are included in this published article.

Acknowledgments

Not applicable.

Funding

This work was financially supported by the National Natural Science Foundation of China (Grant No. 32301722), the Anhui Provincial Natural Science Foundation (Grant No. 2308085QC89), the Natural Science Research Project of Anhui Higher Education Institutions (Grant No. 2025AHGXZK40168), the Young Talent Promotion Project of Anhui Association for Science and Technology (Grant No. RCTJ202424), and the Anhui Agricultural University High-level Talents Introduction Project (Grant No. RC412301).

Declarations

Competing interests

The authors declare that they have no conflict of interest.

Author details

[1]School of Engineering, Anhui Agricultural University, Hefei, Anhui, 230036, China; [2]Department of Biological Systems Engineering, Washington State University, Richland 99354, United States; [3]College of Agricultural Engineering and Food Science, Shandong University of Technology, Zibo, Shandong, 255049, China

References

[1] Chen X, Ren Y, Wang Z. 2025. Advances in transparent electromagnetic interference shielding materials: a review. *Nano Research* 18:94907954

[2] Zhai M, Zhao S, Guo H, Li X, Shi X, et al. 2025. Bionic-structured electromagnetic interference shielding composites. *Science Bulletin* 70:2347−2364

[3] Zhao H, Wang J, He M, Li S, Guo H, et al. 2025. Electromagnetic interference shielding films: structure design and prospects. *Small Methods* 9:2401324

[4] Liu H, Lei F, Xu W, Li Q, Lei C, et al. 2025. Designing carbon-foam composites *via* molten-state reduction for multifunctional electromagnetic interference shielding. *ACS Nano* 19:1198−1210

[5] Liu J, Yu MY, Yu ZZ, Nicolosi V. 2023. Design and advanced manufacturing of electromagnetic interference shielding materials. *Materials Today* 66:245−272

[6] Wang M, Pan X, Wang Y, Wang Q, Wang J, et al. 2026. Multifunctional bilayer Ag NW-ANF nanocomposite films with excellent mechanical and electromagnetic interference shielding properties. *Advanced Functional Materials* 36(45):e75327

[7] Yang W, Pan D, Liu S, Jia G, Wang Y, et al. 2025. Multifunctional wearable conductive nanofiber membrane with antibacterial and breathable ability for superior sensing, electromagnetic interference shielding, and thermal management. *Advanced Functional Materials* 35:2414811

[8] Mohanan R, Balakrishnan R, Shylaja K, Kalarikkal N, Suresh R, et al. 2026. Flexible PEDOT: PSS/PVA/Co_3O_4 nanocomposite films with absorption-dominated EMI shielding performance. *Composites Science and Technology* 278:111554

[9] Zhu H, Fu K, Huang T, Liu H, Yang B, et al. 2024. Highly conductive CFRP composite with Ag-coated T-ZnO interlayers for excellent lightning strike protection, EMI shielding and interlayer toughness. *Composites Part B: Engineering* 279:111448

[10] Chen M, Zhu J, Zhang K, Zhou H, Gao Y, et al. 2024. Carbon nanofiber/polyaniline composite aerogel with excellent electromagnetic interference shielding, low thermal conductivity, and extremely low heat release. *Nano-Micro Letters* 17:80

[11] Zhou Y, Chen M, Xu X, Meng Q, Tu J, et al. 2024. Investigating the effects of γ-ray irradiation on the mechanical and dielectric properties of poly(lactide)/poly(butylene adipate-co-terephthalate)/carbon nanotubes composites. *Advanced Composites and Hybrid Materials* 7:45

[12] Chen J, Guo X, Tan R, Huang M, Ren J, et al. 2025. Achieving the simultaneous improvement of degradation, thermal, and mechanical properties of polylactic acid composite films by carbon quantum dots. *Composites Part B: Engineering* 299:112442

[13] Chen J, Kong C, Tan R, Ren J, Huang M, et al. 2025. Sustainable multiscale interface engineering of bio-based poly(lactic acid) nanocomposite films. *ACS Applied Polymer Materials* 7:15777−15789

[14] Liu T, Feng H, Jin C, Pawlak M, Saeb MR, et al. 2024. Green segregated honeycomb biopolymer composites for electromagnetic interference shielding biomedical devices. *Chemical Engineering Journal* 493:152438

[15] Miao Y, Lin J, Wang E, Liang Y, Li W, et al. 2023. Electrically conductive bamboo charcoal@cellulose nanofibrils based composite membranes designed for electromagnetic interference shielding and flame retardant. *Industrial Crops and Products* 206:117713

[16] Li S, Du Y, Ye H, Wu J, Wang Y, et al. 2024. All-natural self-bonded biocomposite providing superior electromagnetic interference shield performance with effective absorption. *Advanced Functional Materials* 34:2406282

[17] Yu S, Lu Z, Chen L, Xu C, Zhou J, et al. 2026. Electrically conductive wood-based materials beyond biochar: modifications, functions, and environmental impact. *Matter* 9:102528

[18] Yi B, Sun Z, Deng J, Lim JY, Senadheera S, et al. 2026. Sustainably graphitizing biomass into advanced carbon materials for energy and environmental applications. *Sustainable Carbon Materials* 2:e014

[19] Xu L, Si R, Ni Q, Chen J, Zhang J, et al. 2024. Synergistic magnetic/dielectric loss and layered structural design of Ni@carbon fiber/Ag@graphene fiber/polydimethylsiloxane composite for high-absorption EMI shielding. *Carbon* 225:119155

[20] Ren J, Huang C, Tan R, Chen J, Huang M, et al. 2025. All-biomass nanocomposite films *via* facile and sustainable design procedure for thermal management and electromagnetic interference shielding. *Advanced Science* 12(43):e10372

[21] Han W, Wang Y, Wang L, Xie P, Liu T, et al. 2026. A comprehensive review of biomass torrefaction as a versatile platform for the synthesis of functional carbon materials. *Sustainable Carbon Materials* 2:e007

[22] Zhu X, Lin L, Pang M, Jia C, Xia L, et al. 2024. Continuous and low-carbon production of biomass flash graphene. *Nature Communications* 15:3218

[23] Luong DX, Bets KV, Algozeeb WA, Stanford MG, Kittrell C, et al. 2020. Gram-scale bottom-up flash graphene synthesis. *Nature* 577:647−651

[24] Mao X, Zhao P, Liu M, Song J, Cui L, et al. 2026. Graphene-structured biochar produced via Joule heating enhances soil functions, microbial communities, and plant growth. *Journal of Analytical and Applied Pyrolysis* 196:107759

[25] Qiu Y, Su Y, Jing X, Xiong H, Weng D, et al. 2025. Rapid closed pore regulation of biomass-derived hard carbons based on flash joule heating for enhanced sodium ion storage. *Advanced Functional Materials* 35:2423559

[26] Wang F, Huang R, Yu Y, Tan S, Yuan R, et al. 2026. Sustainable production of microalgae-derived turbostratic graphene *via* flash Joule heating. *Bioresource Technology* 442:133729

[27] Xu X, Xu R, Zhao Y, Wu Y, Yuan Q, et al. 2024. Boron-doped biomass carbon nanostructures as electrocatalysts for the two-electron oxygen reduction reaction. *ACS Applied Nano Materials* 7:18912−18919

[28] Tan Z, Mahmood F, Tian M, Li Y, Zhang Q, et al. 2026. Review of flash joule heating for the synthesis of graphene and other functional carbon materials. *Carbon Energy* 8:e70119

[29] Chen J, Tan R, Ren J, Huang M, Wang L, et al. 2025. Polylactic acid (PLA) composites reinforced by end-capped ZnO quantum dots for enhanced mechanical, thermal, and degradation properties. *Polymer* 337:129007

[30] Dehghani A, Arjmand M. 2025. Multi-layered rubber-based nanocomposites for absorption-dominant EMI shielding and adaptive infrared camouflage. *Chemical Engineering Journal* 521:166285

[31] Liu L, Sun Y, Luo H, Ao Y, Jin L. 2026. Boosting EMI Shielding and Joule Heating in Carbon Fiber Paper through lotus seedpod-inspired core-shell nickel nanospheres/ MXene hierarchical reinforcement layer. *Composites Part B: Engineering* 313:113411

[32] Patadia M, Quinn A, Tank M, Jolowsky C, Luiz L, et al. 2024. Enhanced multifunctionality in carbon fiber/carbon nanotube reinforced PEEK hybrid composites: superior combination of mechanical properties, electrical conductivity, and EMI shielding. *Composites Part B: Engineering* 284:111674

[33] Kim SI, Moon JY, Hyeong SK, Ghods S, Kim JS, et al. 2024. Float-stacked graphene – PMMA laminate. *Nature Communications* 15:2172

[34] Wang J, Deng M, Chen H, Qiu W, Duan Y, et al. 2025. Minimizing energy loss by designing multifunctional solid additives to independent regulation of donor and acceptor layers for efficient LBL polymer solar cells. *Advanced Science* 12:2414712

[35] Biswas A, Sapkota PK, Kazibwe S, Yang S, Amiri M, et al. 2026. A semiconductor composite with high solid-state lubrication and low thermal conducting properties. *Advanced Functional Materials* 36:e25251

[36] Parodi A, Vagnoni M, Frontali L, Albonetti C, De Giorgio F, et al. 2023. Bifunctional heterogeneous catalysts from biomass and waste polysaccharides for the conversion of CO_2 into cyclic carbonates. *Journal of Materials Chemistry A* 11:775−788

[37] Nofar M, Zhu W, Park CB. 2012. Effect of dissolved CO_2 on the crystallization behavior of linear and branched PLA. *Polymer* 53:3341−3353

[38] Promhuad K, Ebel L, Harnkarnsujarit N. 2025. Thermoplastic starch/poly(butylene adipate-*co*-terephthalate) blown film with maltol and ethyl maltol preserving cake quality: morphology and antimicrobial function. *Food Chemistry* 464:141646

[39] Yang P, Cao S, Wang Y, Fang B, Zhang S, et al. 2025. Stretch-inducing hierarchical alignment in 3D-printed scaffolds of PLA-based composite and its influence on mechanical properties. *European Polymer Journal* 237:114190

[40] Zeng XR, Zhan R, Xiao Y, Shi LY, Yang KK, et al. 2026. Versatile lignin-enabled dynamic crosslinked networks for mechanically robust and reprocessable PBAT/PLA composites. *Composites Science and Technology* 278:111576

[41] Liu X, Liu Y, Fan M, Qian K, Ma W, et al. 2025. Development of antibacterial starch-based PLA/PBAT active packaging films for enhanced beef preservation. *Food Chemistry* 493:145804

[42] Liu Y, Yang M, Wang J, Yue H, Du Z, et al. 2025. Ag-CNC nanoparticles decorated thermoplastic starch/PLA/PBAT composite film with superior antibacterial property, enhanced barrier capacity and high UV-shielding effect. *Industrial Crops and Products* 225:120510

[43] Liu W, Wang Y, Xiang S, Liu H. 2024. Unveiling the effect of enhanced interfacial compatibility on the mechanical properties of PLA/PBAT blends. *Polymer* 296:126815

[44] Wu S, Du Y, Ning X, Xie F, Xie H, et al. 2026. Efficient fabrication of biodegradable polylactic acid/poly (butylene adipate-co-terephthalate)/titanium dioxide films integrating ethylene catalysis and antibacterial activity for fruits and vegetables preservation. *Food Packaging and Shelf Life* 54:101713

[45] Tran TS, Nguyen SD, Lee HJ, Tran VP. 2023. Advanced crack detection and segmentation on bridge decks using deep learning. *Construction and Building Materials* 400:132839

[46] Ye X, Wang Z, Zhang J, Wan X. 2021. Noncovalently functionalized commodity polymers as tailor-made additives for stereoselective crystallization. *Angewandte Chemie International Edition* 60:20243−20248

[47] Gao S, Ding J, Wang W, Lu J. 2023. Carbon foam/reduced graphene oxide/paraffin composite phase change material for electromagnetic interference shielding and thermal management. *Journal of Energy Storage* 58:106355